Spin splitting and spin Hall conductivity in buckled monolayers of group 14: First-principles calculations

S. M. Farzaneh [*]

Department of Electrical and Computer Engineering, New York University, Brooklyn, New York 11201, USA

Shaloo Rakheja [†]

Holonyak Micro and Nanotechnology Laboratory, University of Illinois at Urbana-Champaign, Urbana, Illinois 61801, USA

Elemental monolayers of group 14 with a buckled honeycomb structure, namely, silicene, germanene, stanene, and plumbene, are known to demonstrate spin splitting as a result of an electric field parallel to their high-symmetry axis, which is capable of tuning their topological phase between a quantum spin Hall insulator and an ordinary band insulator. We perform first-principles calculations based on density functional theory to quantify the spin-dependent band gaps and the spin splitting as a function of the applied electric field and extract the main coefficients of the invariant Hamiltonian. Using linear response theory and the Wannier interpolation method, we calculate the spin Hall conductivity in the monolayers and study its sensitivity to an external electric field. Our results show that the spin Hall conductivity is not quantized and, in the case of silicene, germanene, and stanene, degrades significantly as the electric field inverts the band gap and brings the monolayer into the trivial phase. The electric-field-induced band gap does not close in the case of plumbene with a spin Hall conductivity that is robust to the external electric field.

I. INTRODUCTION

The buckled monolayers of group 14 possess a topological phase known as the quantum spin Hall insulator [1]. An external electric field, via a substrate or a gate contact, provides an experimentally feasible way to tune the spin properties of these materials, which is highly desirable in spintronics applications [2]. Calculations show that an external electric field is capable of switching the topological phase into a trivial band insulating phase [3]. Moreover, it is well known [3,4] that the electric field induces spin splitting in the bands at the K point of the Brillouin zone. However, the impact of the electric-field-induced spin splitting on the quantum spin Hall phase and the spin Hall conductivity is relatively less explored. With the recent experimental realization of stanene [5] and plumbene [6], it is desirable to investigate the impact of the electric field on the spin splitting and, consequently, the spin Hall conductivity via systematic first-principles calculations based on density functional theory and linear response theory.

Elemental monolayers of group 14 of the periodic table are two-dimensional (2D) crystals of carbon, silicon, germanium, tin, and lead, which are known as graphene, silicene, germanene, stanene, and plumbene, respectively. This family of 2D materials possesses a variety of properties ranging from Dirac energy dispersion of the low-energy excitations at the K point and a spin-orbit-induced band gap to the possibility of

a quantum spin Hall insulating phase which is tunable via an external electric field [7]. Following the successful isolation of graphene a decade ago [8], other members of this family came into existence, starting with silicene [9–12], which was followed by germanene [13,14] and, more recently, by stanene [5,15,16] and plumbene [6]. In their most stable configuration, they show a buckled honeycomb structure which possesses a lower symmetry than that of graphene. Therefore, in general, the electronic states are expected to have a lower number of degeneracies. Since these monolayers consist of elements heavier than carbon, spin-orbit coupling is expected to affect the electronic band structure more significantly. In fact, as one goes from silicene to plumbene, the intrinsic band gap at the K point increases, and the Fermi velocity decreases.

Spin-orbit coupling in the buckled monolayers is of essential importance both in fundamental physics such as the quantum anomalous Hall effect [17,18] and the quantum spin Hall effects [3,19] and also in spintronics applications such as the spin-polarized transistor [20], spin-valley logic [21–23], spin filter [2,24], valley-polarized metal [25], and electrical switching of magnetization via spin-orbit torques [26]. Rich literature exists on theoretical works on buckled monolayers in the past decade based on group theoretic works [4,27,28], effective Hamiltonians [3,28–32], and first-principles calculations based on density functional theory [2,29,30,33–45]. Nevertheless, only a few first-principles works [2,36,37,40] studied the effect of the electric field in buckled monolayers. Of these studies, only Refs. [2,36] include the relativistic spin-orbit coupling effects. *Ab initio* studies [46–48] on the spin Hall conductivity of germanene and stanene have only recently become available. Here, we go a step further by
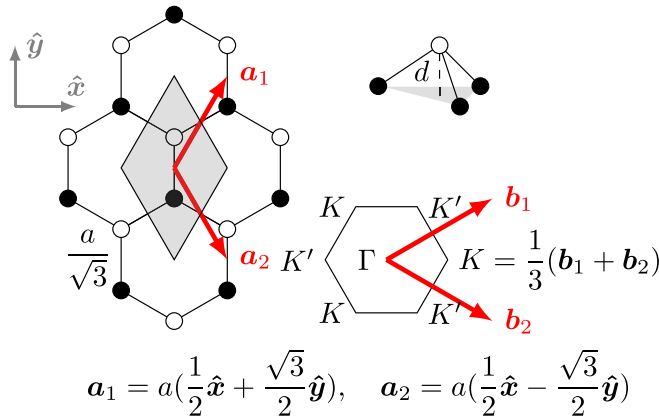

FIG. 1. A two-dimensional buckled honeycomb crystal with lattice constant a and buckling size d. The primitive unit cell is shaded in gray, and the primitive vectors are drawn in red. Dark and light circles denote atoms on different sublattices. The first Brillouin zone along with the reciprocal vectors is shown in the bottom right.

analyzing the electronic properties of all the monolayers: silicene, germanene, stanene, and plumbene. For each monolayer, we systematically investigate the effect of electric-field-induced spin splitting in conjunction with the spin Hall conductivity via fully relativistic first-principles calculations for a wider range of electric fields and energies than in previous works [2,47]. We quantify various spin properties of the buckled monolayers such as the spin splitting, spin-dependent band gaps, critical electric field required for topological phase transition, coefficients of the low-energy invariant Hamiltonian, and spin Hall conductivity with and without the electric field.

A brief group theoretic analysis of the bands at the K point is provided in Sec. II, where we show how the symmetry classification of the bands changes as the spin-orbit coupling, the buckling, and the electric field are introduced one by one. First-principles calculations of the band structure and the spin-split bands of the monolayers are studied in detail in Sec. III, where the effect of the external electric field is taken into account in the self-consistent Kohn-Sham equations. The coefficients of an invariant Hamiltonian describing the low-energy band structure at the K point are extracted in Sec. IV. The spin Hall conductivity of the monolayers is calculated and discussed in Sec. V. The paper concludes with a summary of key findings and outlook in Sec. VI.

II. CRYSTAL STRUCTURE AND SYMMETRIES

The crystal structure of the monolayers of group 14 consists of atoms arranged in a honeycomb structure, as shown in Fig. 1. The honeycomb structure can be thought of as a Bravais lattice with a basis of two atoms, i.e., dark and light circles in Fig. 1. The dark and light circles each consist of a triangular Bravais lattice by themselves. In general, an out-of-plane buckling in the honeycomb structure can exist depending on the relative stability of the sp^2 and sp^3 hybridizations as well as the exchange-correlation potentials [33]. The buckling size, denoted by d, is the distance between the two triangular sublattices. The buckling is zero
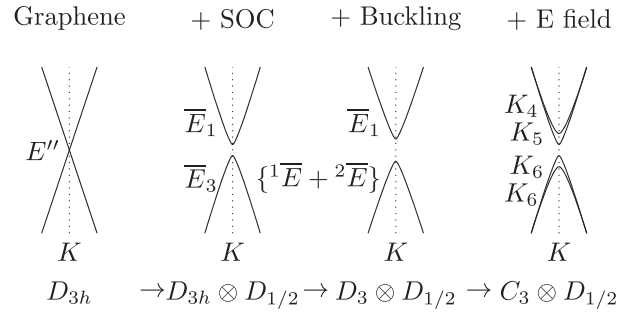

FIG. 2. Symmetry classification of the Dirac point with respect to the group of the wave vector at the K point. As one goes from spinless graphene to the buckled monolayers in the presence of the spin-orbit coupling and the external electric field, different symmetries are introduced or broken, and consequently degeneracies and symmetry properties change.

in the case of planar graphene but increases monotonically as one goes from the lighter to the heavier elements of group 14. The first Brillouin zone of the honeycomb structure is also shown in Fig. 1, where the nonequivalent high-symmetry points on the boundary of the Brillouin zone, K and K', host the low-energy excitations. The symmetry of planar graphene is classified by the symmorphic space group $P6/mmm$ (No. 191), which is homomorphic to point group D_{6h}. The buckled monolayers have a lower symmetry than that of graphene because the sixfold rotational symmetry reduces to a threefold one and the horizontal mirror symmetry is broken as well. However, they retain the inversion symmetry. Their symmetry is classified by space group $P\bar{3}m1$ (No. 164) with the corresponding point group D_{3d}, which is a subgroup of D_{6h}. Although Ref. [28] studied the global symmetry properties of graphene systems, here, we focus on the symmetry properties of the K point in the Brillouin zone.

Group theoretic arguments can provide insight into the qualitative behavior of the bands such as the number of degeneracies and how or if they are lifted as the symmetry is lowered. The details of the symmetry analysis and the symmetry tables are provided in the Supplemental Material [49]. Here, the symmetry properties are briefly mentioned. Figure 2 illustrates the qualitative behavior of the bands in the vicinity of the K point. It illustrates how the irreducible representations (IRs) of the bands at the Dirac point change. Specifically, the degeneracies are lifted as one goes from graphene to other lower-symmetry materials in the presence of buckling and an external electric field. Each step is denoted by a point group corresponding to the group of the wave vector at the K point. Starting from spinless graphene with point group D_{3h}, the Dirac point is labeled with E'', a two-dimensional IR which implies a twofold degeneracy at the Dirac point [50]. The effect of the spin-orbit coupling can be shown by using the double group representations which are obtained by the direct product of the point group with the spinor representation $D_{1/2}$, i.e., $D_{3h} \otimes D_{1/2}$. The IRs of this double group are at most two-dimensional. Therefore, no fourfold degeneracy (including spins) is allowed at the Dirac point, and therefore, a gap opens up. After the inclusion of spinors with the representation $\overline{E}$, the IR of the bands at the Dirac point changes to $E'' \otimes \overline{E} = \overline{E}_1 + \overline{E}_3$, which are two twofold bands. The

TABLE I. Parameters in the setup of the first-principles calculations.

	C	Si	Ge	Sn	Pb
Wave function E_{cut} (Ry)	40	45	50	70	46
Charge density E_{cut} (Ry)	326	180	200	280	211
Number of bands	16	16	16	36	36
Energy convergence threshold (a.u.)			10^{-8}		
Force convergence threshold (a.u.)			10^{-7}		
Number of Wannier orbitals			8		

Calculation	No. of k points
Structural optimization	$12 \times 12 \times 1$
Self-consistent field	$48 \times 48 \times 1$
Band structure k path	150
Density of states	$96 \times 96 \times 1$
Wannier interpolation	$800 \times 800 \times 1$

buckling breaks some of the symmetries of the planar graphene structure such as the in-plane mirror symmetry and the sixfold rotational symmetries resulting in point group D_3. No degeneracy is lifted as the buckling is introduced and the bands are represented with the same twofold degeneracy but with labels according to point group D_3, i.e., $\overline{E}_1(D_{3h}) \rightarrow \overline{E}_1(D_3)$ and $\overline{E}_3(D_{3h}) \rightarrow \{^1\overline{E} + ^2\overline{E}\}(D_3)$. The electric field reduces the symmetry further to point group C_3, which contains only one-dimensional representations, and therefore, all degeneracies are lifted. Although group theory can predict the spin splitting, the ordering and the energy of the bands are obtained only through calculations or experiments.

III. FIRST-PRINCIPLES CALCULATIONS

First-principles calculations based on density functional theory are performed via the QUANTUM ESPRESSO suite [51,52]. The projector augmented wave method [53], which generalizes the pseudopotential method, is used to improve the computational efficiency. The pseudopotential files were obtained from Ref. [54]. Scalar-relativistic pseudopotentials are used for structural relaxation, whereas fully relativistic pseudopotentials are used to capture spin-orbit coupling effects. The exchange-correlation functional utilizes the generalized gradient approximation [55]. Other parameters and details of the first-principles setup are presented in Table I.

The lattice parameters are obtained with the structural optimization using the Broyden-Fletcher-Goldfarb-Shanno algorithm, which is a quasi-Newton optimizer in which the forces are calculated using the Hellmann-Feynman theorem. The optimized lattice parameters, such as the lattice constant and the buckling height, which minimize the total force and stress, are listed in Table II. As seen from Table II, the values are similar to the ones reported previously in the literature [2,29,34]. The supercell contains a 20 Å vacuum to avoid fictitious interlayer interaction due to the periodic boundary condition. The external electric field is modeled as an effective sawlike potential which is added directly to the self-consistent Kohn-Sham equations. The magnitude of the homogeneous electric field, which is perpendicular to the crystal plane, is

TABLE II. Optimized structural parameters of graphene, silicene, germanene, stanene, and plumbene, i.e., the lattice constant a and the buckling size d as defined in Fig. 1.

	C	Si	Ge	Sn	Pb
a (Å)	2.466	3.868	4.022	4.652	4.924
d (Å)	0.000	0.453	0.687	0.862	0.939

increased gradually to ease the convergence. The pressure of the crystal is kept below 0.5 kbar. The nonzero pressure is mostly due to the periodicity in the direction perpendicular to the crystal plane and can be reduced by increasing the vacuum size further. However, its effect on the optimized lattice constant is negligible, i.e., 0.001 Å for a vacuum twice as large.

The fully relativistic band structures of graphene, silicene, germanene, and stanene along with their densities of states are illustrated in Fig. 3. The bands shown in the energy window are composed of only s and p orbitals as the d orbitals, in the case of germanene, stanene, and plumbene, are narrow and localized far below the Fermi energy. The density of states approaches zero at the Fermi energy due to the band gap caused by the spin-orbit coupling effects. The density of states of
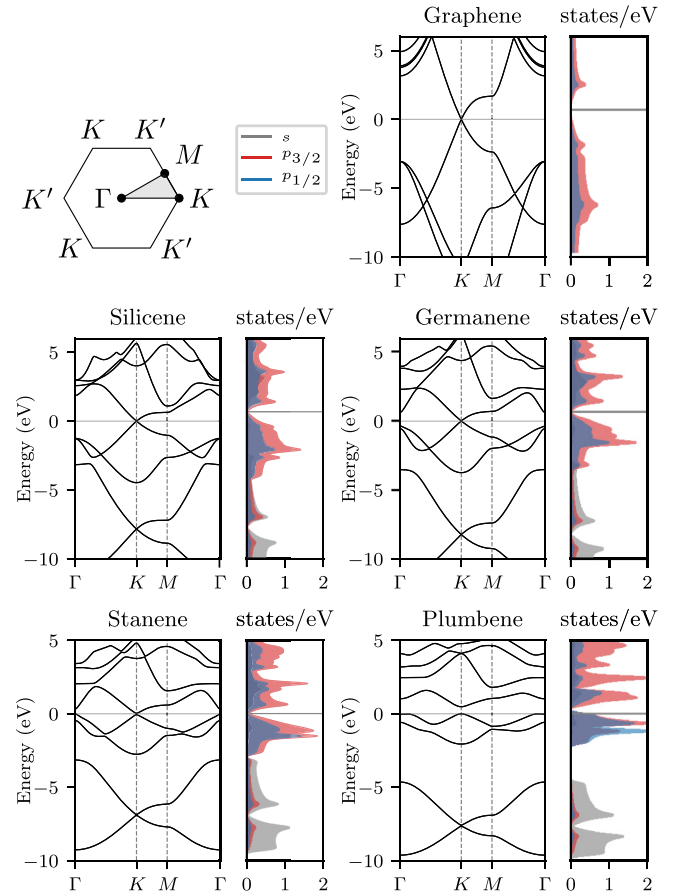

FIG. 3. The band structures of graphene, silicene, germanene, stanene, and plumbene along with their corresponding densities of states (DOS) in 1/eV units. The energy axis is relative to the Fermi energy denoted by the gray horizontal line.
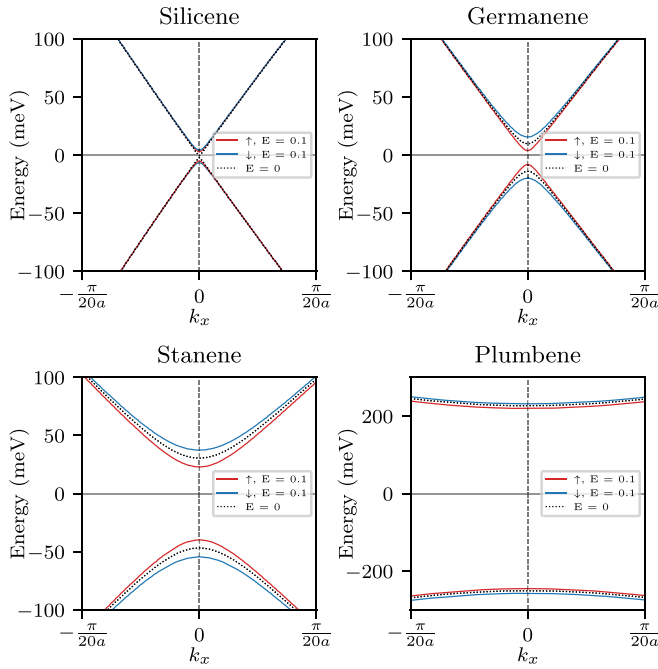
FIG. 4. The effect of the electric field on the band structures of silicene, germanene, stanene, and plumbene at the K point of the Brillouin zone along the x direction. The energy axis is relative to the Fermi energy denoted by the gray horizontal line. The spin splitting and the change in the band gap depend on the relative strength of the electric field and the spin-orbit coupling. The electric field is in V/Å.

FIG. 5. The spread of the spin splitting induced by the electric field ($E = 0.1$ V/Å) in the vicinity of the K point for silicene, germanene, stanene, and plumbene.

band as a function of the electric field. The general behavior of the spin-dependent band gap is that the spin-down band gap linearly increases, whereas the spin-up band gap initially decreases until it reaches zero or the valley polarized metal state [25] and then increases again. It has been shown [3] that a topological phase transition occurs at the zero-gap point, therefore changing the topological phase from a quantum spin Hall insulator to an ordinary band insulator. The transition does not occur for plumbene in the field range shown in Fig. 6. Higher-order effects, due to the stronger spin-orbit coupling in plumbene, emerge at around $E = 0.8$ V/Å, which stops the gap from closing and making the transition. The transition for silicene happens at a relatively smaller electric field of $E = 0.018$ V/Å, compared to that of germanene, $E = 0.21$ V/Å, and that of stanene, $E = 0.56$ V/Å. This suggests that germanene and stanene might be better candidates for any

graphene is more dispersed due to its higher bandwidth compared to other monolayers. The band gap of graphene is very small, of the order of μeV, due to the weak atomic spin-orbit coupling of carbon atoms. The resulting band gaps of silicene, germanene, stanene, and plumbene are 1.5, 23.7, 77.2, and 477 meV, respectively. There is a good match between these values and the ones reported before [2,29]. In the presence of an electric field the inversion symmetry of the crystal is broken, and the degeneracies of the bands at the K and K' points are lifted. Figure 4 depicts the spin-split bands in the vicinity of the K point with and without an external electric field. The energy window for plumbene is chosen to be larger than the rest to capture the band gap. The band gap without an electric field is a result of the intrinsic spin-orbit coupling, which is stronger for the monolayers with heavier elements. We note that the energy band diagram looks the same for the K' point except that the spins are the opposite of that at the K point due to the time reversal symmetry, i.e., $E_\uparrow(K) = E_\downarrow(K')$. The spin splitting is not uniform across the k space. It peaks at the K point and decays outward. The spread of the splitting is also not the same for different monolayers. Figure 5 shows the spread of spin splitting close to the K point in the presence of an electric field with a magnitude of 0.1 V/Å. As seen from Fig. 5 the heavier the element is, the stronger the spin-orbit coupling is, and the larger the band gap is, which in turn corresponds to a heavier effective mass and therefore a more widely spread spin splitting. To investigate the impact of the electric field more closely we calculate the band structure for a wide range of electric field magnitudes. Figure 6 plots the spin-up and spin-down band gaps along with the spin splitting of each
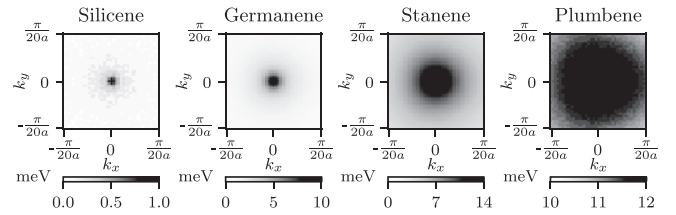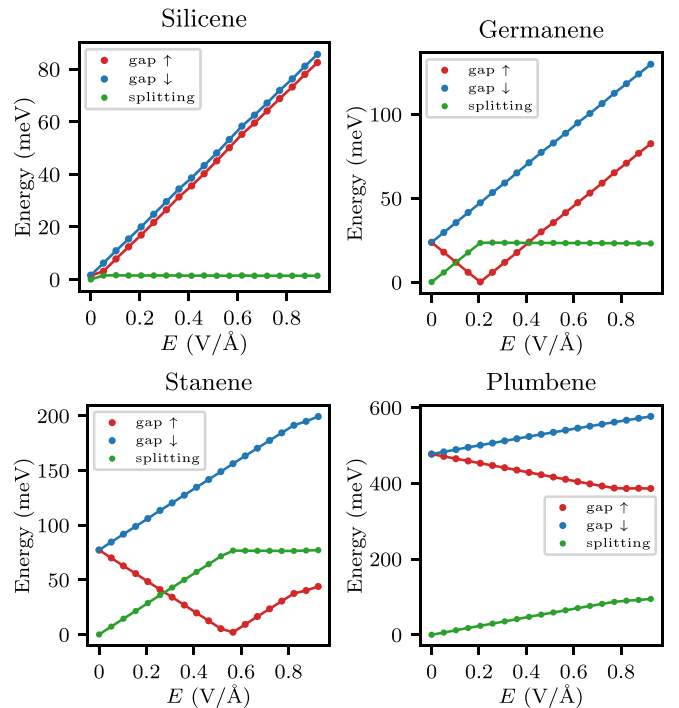

FIG. 6. The spin-dependent band gap and the spin splitting as a function of the external electric field for silicene, germanene, stanene, and plumbene. The spin-up band gap closes at the critical electric field. Germanene and stanene show a band inversion at the critical field, whereas no transition happens for silicene and plumbene.
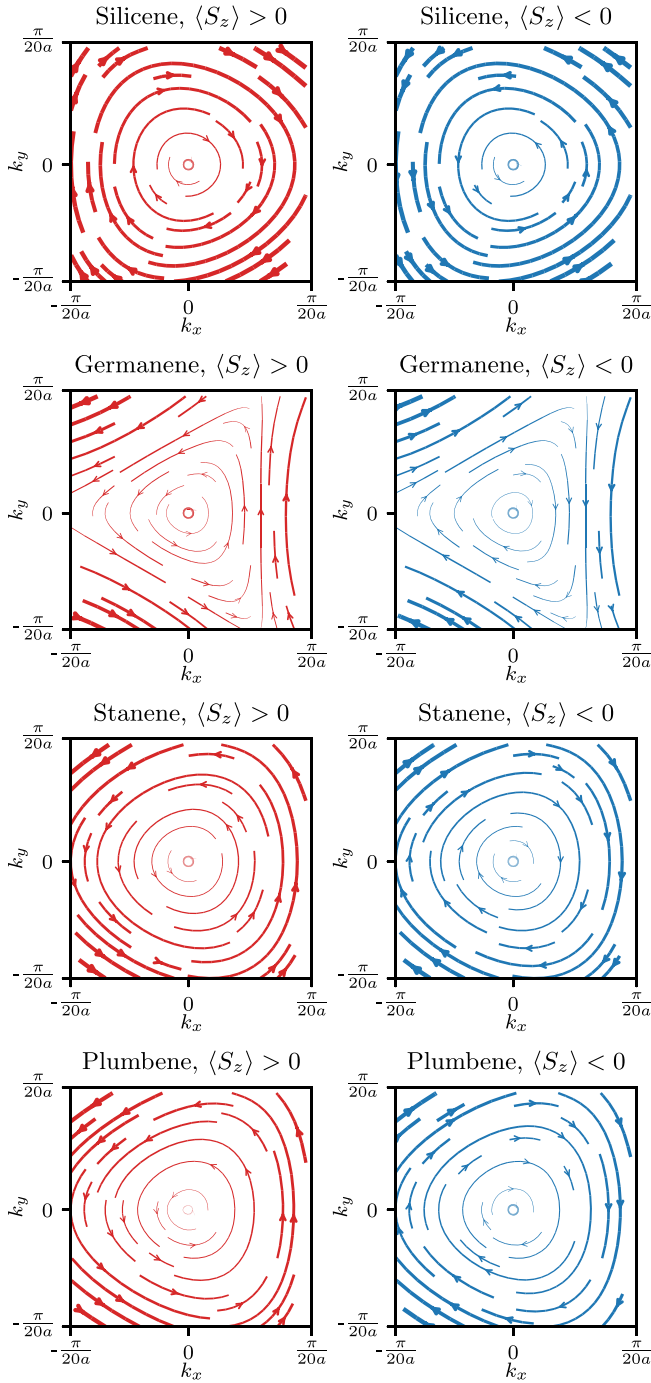
FIG. 7. The in-plane spin texture in the vicinity of the K point. The thickness of the curves is proportional to the magnitude of the in-plane spin projection. The electric field is set to $E = 0.1$ V/Å.

device application based on the topological phase transition as silicene might be easily pushed into its trivial regime due to the substrate-induced electric field [43]. We note that the spin splitting stops increasing right at the transition field and saturates to a value equal to the intrinsic band gap. The upper bound on the spin splitting results from the intrinsic spin-orbit coupling of the crystal, as shown elsewhere [56].

The electric field introduces Rashba-like spin-orbit coupling, which in turn leads to an in-plane spin texture. Figure 7

illustrates the expectation value of the in-plane spin projection in the presence of an electric field with magnitude $E = 0.1$ V/Å in the vicinity of K. The left and right columns correspond to the two spin-split conduction bands, which are highly spin-polarized in the z direction, i.e., $\langle S_z \rangle \approx \pm \hbar/2$. At this specific value of the electric field, silicene, which is in the trivial insulator phase, shows a spin projection opposite to the rest of the monolayers. Germanene shows a significant trigonal warping in the spin texture which indicates that the higher-order spin-orbit terms are more pronounced in germanene than in other monolayers. As we will see in Sec. V, these spin-orbit terms are responsible for the deviation of the spin Hall conductivity from the quantized value.

IV. EFFECTIVE HAMILTONIAN

The theory of invariants provides a systematic approach for obtaining an effective Hamiltonian which is expanded to the desired order in terms of the wave vector $\boldsymbol{k}$, the spin $\boldsymbol{s}$, and the external electric field $\mathcal{E}$ [57]. In general, the terms appearing in the invariant expansion are the various tensor products of $\boldsymbol{k}$, $\boldsymbol{s}$, and $\mathcal{E}$ that are invariant under the symmetry operations of the point group and therefore transform according to the identity representation. The coefficients of the invariant expansion are quantified by first-principles calculations or experiments. Here, we utilize a 4×4 effective Hamiltonian which contains invariant terms that are at most linear in $\boldsymbol{k}$, $\boldsymbol{s}$, and $\mathcal{E}$. This effective Hamiltonian was derived by Geissler *et al.* [4] for silicene in the presence of the spin-orbit coupling and the electric field. The basis of the Hamiltonian consists of two spin and two sublattice states. The effective Hamiltonian resulting from the invariant expansion is $\mathcal{H}(\boldsymbol{k}) = \mathcal{H}_0(\boldsymbol{k}) + \mathcal{H}_\mathcal{E}(\boldsymbol{k})$, where $\mathcal{H}_0(\boldsymbol{k})$ is the Hamiltonian without the external electric field,

$$\mathcal{H}_0(\boldsymbol{k}) = a_1 \tau_z \sigma_z s_z + a_2(\tau_z k_x \sigma_x + k_y \sigma_y) + a_3 \sigma_z (s_x k_y - s_y k_x). \tag{1}$$

Here, $\tau_z = \pm 1$ denotes the K and K' nonequivalent valleys, respectively. The Pauli matrices σ_i and s_i operate in the sublattice and spin spaces. The coefficients $a_1 = \Delta_{SO}/2$, $a_2 = \hbar v_F$, and a_3 are interpreted as the spin-orbit band gap, the Fermi velocity, and a Rashba-like spin-orbit coupling term [28,29] which also introduces some corrections to the Fermi velocity. In the current section we do not list the values for a_3 but provide the values of the spin-orbit gap and the Fermi velocity. The Hamiltonian is modified in the presence of the electric field by $\mathcal{H}_\mathcal{E}(\boldsymbol{k})$ as follows:

$$\begin{aligned}
\mathcal{H}_\mathcal{E}(\boldsymbol{k}) = {} & a_4 \sigma_z s_0 \mathcal{E}_z + a_5 \tau_z \sigma_0 s_z \mathcal{E}_z + a_6 \sigma_0 (s_x k_y - s_y k_x) \mathcal{E}_z \\
& + a_7 (\tau_z \sigma_x s_y - \sigma_y s_x) \mathcal{E}_z + a_8 (\sigma_x k_x + \tau_z \sigma_y k_y) s_z \mathcal{E}_z \\
& + a_9 (\sigma_x (s_x k_y + s_y k_x) + \tau_z \sigma_y (s_x k_x - s_y k_y)) \mathcal{E}_z. \tag{2}
\end{aligned}$$

The terms proportional to a_4 and a_5 represent the electric-field-induced spin splitting. The a_4 term introduces a spin splitting close to only the K point, whereas the spin splitting by the a_5 term is almost independent of the value of k. From the first-principles band structure in the previous section we know that the splitting decreases moving away from the K point. Therefore, it is reasonable to assume that $a_4 \gg a_5$. Hence, we quantify only the a_4 coefficient. The term a_6 represents a Rashba-like energy shift which displaces the

TABLE III. Coefficients a_1-a_4 of the effective Hamiltonian given by the invariant expansion in Eqs. (1) and (2) and extracted by fitting the DFT results for different monolayers.

	Silicene	Germanene	Stanene	Plumbene
a_1 (eV)	0.0007	0.0119	0.0386	0.2385
a_2 (eV Å)	3.499	3.177	2.783	1.599
v_F (10^5 m/s)	5.316	4.827	4.228	2.429
a_3 (eV Å)	0.009	0.069	0.46	0.85
a_4 (eV Å)	0.0417	0.0564	0.0689	0.0589

spin-polarized bands horizontally. Similarly, since the horizontal shifts in the first-principles band structure are negligible, we have $a_4 \gg a_6$. Finally, the terms a_7, a_8, and a_9 represent higher-order corrections to the spin-splitting and the Fermi velocity. Although symmetry allows many terms in the invariant expansion, four coefficients, a_1, a_2, a_3, and a_4, are sufficient to describe the four low-energy bands in the vicinity of the K point. These coefficients for silicene, germanene, stanene, and plumbene are listed in Table III. These values are mostly in accordance with the ones previously reported [2,29]. As seen from Table III, heavier elements show a relatively larger intrinsic band gap, a lower Fermi velocity, and a stronger spin-orbit coupling. However, the electric-field-induced spin-splitting denoted by a_4 shows similar values for different monolayers. We note that the values of a_4 are considerably smaller than a value one would estimate by assuming a bare electric potential, that is, $\Delta_{SO}/\mathcal{E}d$. This is mainly due to the screening of the electric field by the carriers, which in turn leads to carrier redistribution between the sublattice layers and, consequently, reduces the effectiveness of the external electric field. The effective Hamiltonian is valid as long as the higher-order effects of the electric field are not present, that is, $E < 0.8$ V/Å.

We note that there are different numbers reported in the literature for the Rashba parameter of stanene. For instance, Ref. [29] reports a Rashba parameter of $a\lambda_R = 0.045$ eV Å, whereas Ref. [2] reports $a\lambda_R = 0.088$ eV Å. These numbers are an order of magnitude smaller than the value reported in our work, i.e., 0.46 eV Å. Although the values obtained for silicene and germanene are comparable to the ones in the literature, the discrepancy in the case of stanene could result from a different method used to fit the effective model to the *ab initio* results. Since the a_3 term does not change the band gap or the Fermi velocity of the bands, we resorted to the expectation value of the in-plane spin operators to fit the a_3 parameters, which might not be the case in other works. While other parameters of the model are more or less similar to the ones reported before, the Rashba values seem not to be conclusive and require further investigation.

V. SPIN HALL CONDUCTIVITY

The spin Hall conductivity is a linear response coefficient that describes a spin current as the response of the system to an applied electric field. It can be calculated by using the Kubo formula in terms of a Berry-like curvature $\Omega^\gamma_{\alpha\beta,n}(\boldsymbol{k})$,

also called the spin Berry curvature, as follows [58]:

$$\sigma^\gamma_{\alpha\beta} = -\left(\frac{e^2}{\hbar}\right)\left(\frac{\hbar}{2e}\right)\int \frac{d^3\boldsymbol{k}}{(2\pi)^3}\sum_n f(\epsilon_{n,\boldsymbol{k}})\Omega^\gamma_{\alpha\beta,n}(\boldsymbol{k}), \quad (3)$$

where $f(\epsilon_{n,\boldsymbol{k}})$ is the Fermi-Dirac distribution function. The spin Berry curvature is given as

$$\Omega^\gamma_{\alpha\beta,n}(\boldsymbol{k}) = \hbar^2\sum_{m\neq n}\frac{-2\,\mathrm{Im}\{\langle n\boldsymbol{k}|\mathcal{J}^\gamma_\alpha|m\boldsymbol{k}\rangle\langle m\boldsymbol{k}|v_\beta|n\boldsymbol{k}\rangle\}}{(\epsilon_{n,\boldsymbol{k}} - \epsilon_{m,\boldsymbol{k}})^2}, \quad (4)$$

where v_β is the velocity operator and $\mathcal{J}^\gamma_\alpha = \{v_\alpha, \sigma_\gamma\}/2 = (v_\alpha\sigma_\gamma + \sigma_\gamma v_\alpha)/2$ is the spin velocity operator.

Using the effective Hamiltonian derived in the last section, we first calculate the contribution of the Dirac bands at the Fermi level to the spin Hall conductivity. In doing so, we assume that the dominant contribution to the spin Hall conductivity comes from the K point. As we will see, this assumption might not hold true as the low-energy levels appear at the Γ point as well for stanene. Nevertheless, since the electric field induces the band inversion only at the K point, it is still useful to provide an estimate of the spin Hall conductivity from the Dirac bands. The Hamiltonian of the system, considering the distant bands in the vicinity of the K point, is

$$H = \begin{pmatrix} H_0(\boldsymbol{k}) & H_{01}(\boldsymbol{k}) \\ H_{10}(\boldsymbol{k}) & H_1(\boldsymbol{k}) \end{pmatrix}, \quad (5)$$

where $H_0(\boldsymbol{k})$ is the effective Hamiltonian given in Eq. (1), $H_1(\boldsymbol{k})$ represents the distant bands, and $H_{01}(\boldsymbol{k})$ is the interaction between the low-energy bands and the distant bands. Assuming that the distant bands are interacting only weakly, which might not be true in general, it can be shown from the Löwdin partitioning that the effect of the distant bands is quadratic in the leading order. That is,

$$\tilde{H}(\boldsymbol{k}) = H_0(\boldsymbol{k}) + \mathcal{O}\big(H^2_{01}(\boldsymbol{k})\big). \quad (6)$$

Considering only the $H_0(\boldsymbol{k})$ term, the spin Hall conductivity can be obtained from the Kubo formula as worked out in [59]:

$$\sigma^z_{xy} = \frac{a^2_2}{a^2_2 + a^2_3}\frac{e}{4\pi}, \quad (7)$$

where a_2 and a_3 correspond to the Fermi velocity and the intrinsic spin-orbit coupling and are given in Table III. A spin-orbit coupling term that is much smaller than the Fermi velocity term, i.e., $a_3 \ll a_2$, results in a quantized spin Hall conductivity σ^z_{xy} in units of $e/4\pi$ as predicted before in the literature [46,47,59]. As we discuss next, the spin Hall conductivity calculated from first principles within the density functional theory is not quantized in $e/4\pi$. This discrepancy suggests that the assumptions made in the derivation of Eq. (7) may not be correct; that is, the coupling to the distant bands contributes significantly to the spin Hall conductivity. We note that even if the Hamiltonian is completely diagonalized, the contributions from the matrix elements of the velocity operator are still present as the energy eigenstates are not simultaneously eigenstates of the velocity operator as well. Therefore, a complete picture of the spin Hall effect in these materials requires us to incorporate a full band Hamiltonian. We do so by performing first-principles calculations based on density functional theory.

We note that earlier works in the literature calculated the spin Hall conductivity of germanene [46] and stanene [47] at the Fermi level. We go a step further by including silicene and plumbene in our calculations as well as providing results for a wide range of energies and for several values of the external electric field.

The spin Hall conductivity is, in general, a tensor of rank 3 with 27 components. However, one need not calculate all the components as symmetry simplifies the calculations by relating the components to each other. The space group of the buckled monolayers, $P\bar{3}m1$, corresponds to the magnetic Laue group $\bar{3}m11'$. According to this symmetry classification, it can be shown that the number of independent tensor components reduces to four [60]. Out of these four components, $\sigma_{xy}^z = -\sigma_{yx}^z$ dominates the rest. This is, in fact, the component corresponding to the quantum spin Hall effect. Here, we calculate σ_{xy}^z for the buckled monolayers over a wide range of energies. To evaluate Eq. (3), we use the Wannier interpolation method [61–63] recently implemented in the WANNIER90 code [62,64]. This method takes advantage of the smoothness of the maximally localized Wannier gauge to integrate the spin-Berry curvature over the Brillouin zone. The results are shown in Fig. 8, where the spin Hall conductivity is in units of $e/4\pi = (e^2/h)(\hbar/2e)$.

The plots in the left column show σ_{xy}^z in the absence of the external electric field, and therefore, the bands are not spin split. As seen from Fig. 8, the values of σ_{xy}^z at the Fermi energy are not quantized. The quantization value is in units of $e/4\pi$. The values for silicene, germanene, stanene, and plumbene at the Fermi level are $\sigma_{xy}^z =$ 0.20, 1.05, 1.80, and 3.41, respectively. These values suggest that the heavier the element is, the higher spin Hall conductivity it shows at the Fermi energy. This behavior is consistent with previous calculations for three-dimensional topological insulators [46,65]. The reason that σ_{xy}^z is not quantized is, in general, due to terms that do not conserve spin s_z, as pointed out in the literature [1,47]. From the invariant Hamiltonian in Eqs. (1) and (2) one can see that $[\mathcal{H}, s_z] \neq 0$ due to the existence of Rashba-like terms such as the term with coefficient a_3. It is worth mentioning that the a_3 term is a result of the buckling and is not present in planar structures such as graphene [57], which shows a quantized spin Hall conductivity. Although a significant a_3 term in Eq. (7) could explain a spin Hall conductivity that is smaller than $e/4\pi$ in a Dirac band model, it cannot describe the corresponding values of stanene and plumbene which are greater than $e/4\pi$. As mentioned, this pertains to the fact that the contributions of the other bands below the Fermi level are not negligible. Moreover, as seen from Fig. 9, which illustrates the k-resolved spin Berry curvature, contributions from other points in the Brillouin zone such as the Γ point in stanene also contribute to the spin Hall conductivity.

The behavior of the spin Hall conductivity in the presence of an electric field depends on the topological phase of the system. The right column of Fig. 8 illustrates σ_{xy}^z in the close vicinity of the Fermi level for several values of the electric field where the magnitude of the electric field is changed in steps of 0.1 V/Å. Our general observation is that for electric fields less than the critical value the spin Hall conductivity at the Fermi energy remains the same. As the electric field nears the critical value and goes beyond it, the spin Hall
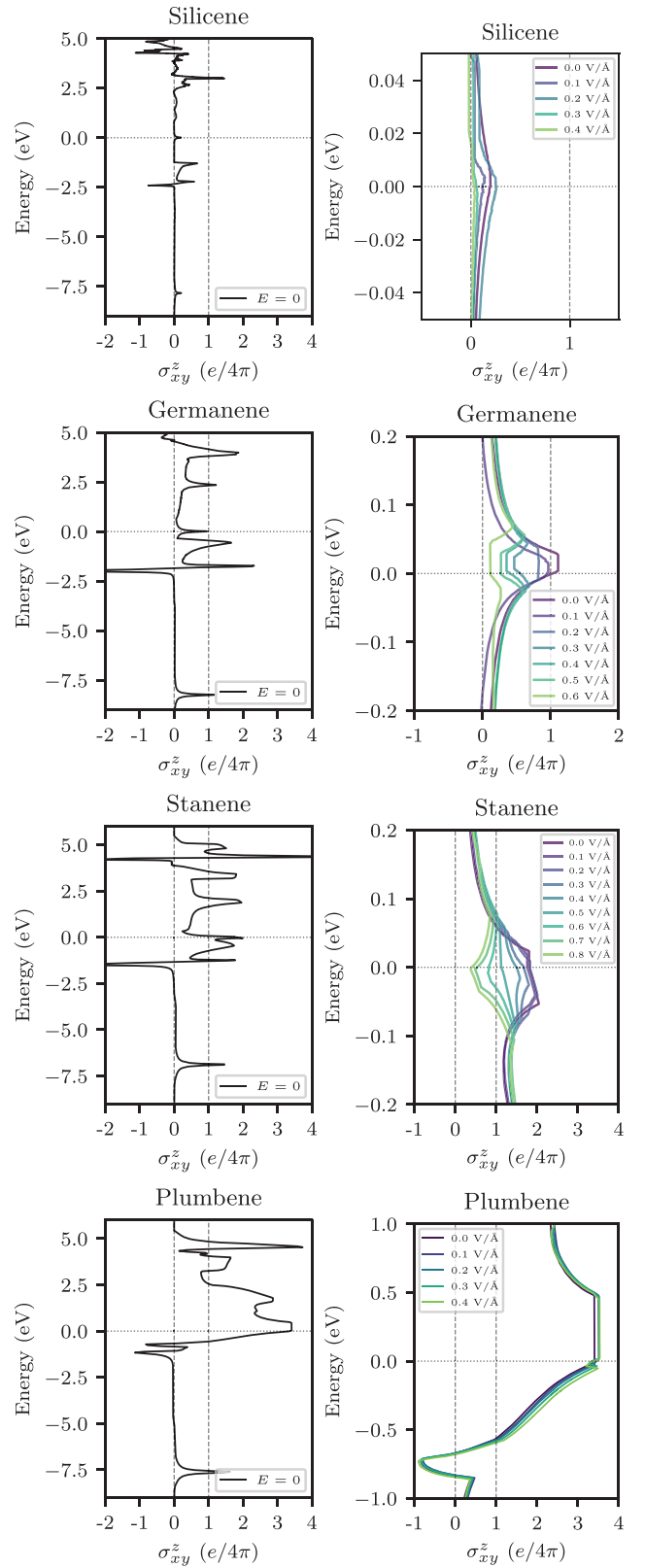

FIG. 8. Spin Hall conductivity as a function of the Fermi energy for different values of the electric field for silicene, germanene, stanene, and plumbene. The left column shows the SHC for a wide range of energies, whereas the right column contains zoomed-in plots in the vicinity of the Fermi energy. The electric field is changed in 0.1 V/Å increments.
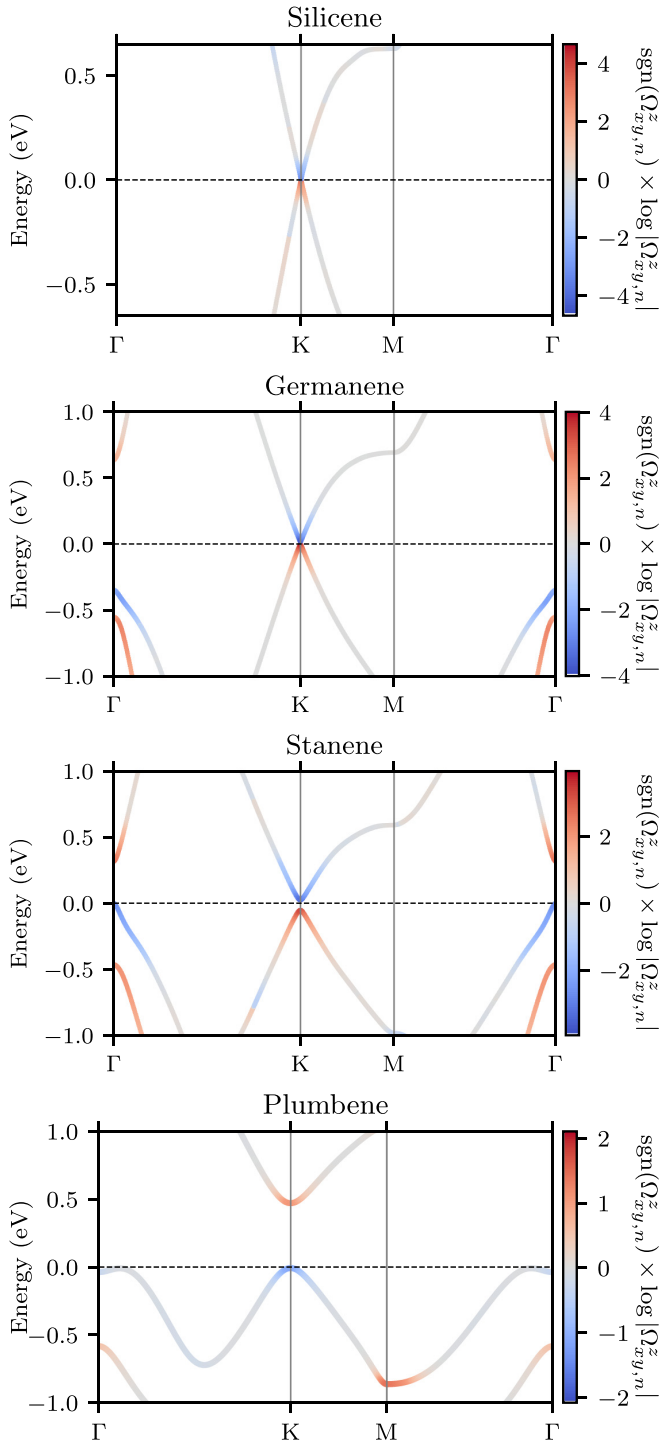
FIG. 9. k-resolved contribution to the spin-Berry curvature for silicene, germanene, stanene, and plumbene.

conductivity degrades significantly. This is the result of field-dependent terms in the invariant Hamiltonian in Eq. (2) which introduce additional spin mixing and therefore degrade the s_z conservation. From a lattice point of view, the switching of the topological phase to the trivial phase by the electric field can be interpreted as the point where the asymmetry between the sublattices outweighs the intrinsic spin-orbit coupling. As a consequence, the ground state changes from the linear com-

bination of different sublattices to a single sublattice with both spins. Therefore, the system does not consist of two copies of the integer quantum Hall state [1] anymore, and the quantum spin Hall phase is destroyed. As seen from Fig. 8 the value of σ_{xy}^z at the Fermi energy for silicene, germanene, and stanene, in the presence of an electric field greater than the critical value, decreases significantly, whereas the value for plumbene that has no critical value remains the same. This shows that the topological quantum spin Hall phase and the spin Hall conductivity in plumbene are robust to the perpendicular electric field, which can be beneficial for spin generation device applications with robustness to the external field effects. On the other hand, silicene, germanene, and stanene could be suitable candidates for device applications requiring switching between the topological and trivial phases. It is worth mentioning that the spin Hall conductivity of stanene does not seem to be constant inside the gap as the electric field is increased. The main reason is that the actual gap is smaller than the gap at the K point. This is due to the fact that the valence band at the Γ point has a slightly higher energy than the top of the valence band at the K point, resulting in an indirect band gap.

VI. CONCLUSIONS

By performing systematic first-principles calculations based on density functional theory we calculated the fully relativistic band structure of the buckled monolayers of group 14 with and without an external electric field. Various spin properties of the monolayers, such as the spin splitting, spin-dependent band gaps, coefficients of the invariant Hamiltonian, and spin Hall conductivity, were calculated. The main result of this work is the energy-dependent spin Hall conductivity of the buckled monolayers for various values of the electric field. Our results show that in contrast to the prediction of the simplified two-band Dirac Hamiltonian [59], the spin Hall conductivity is not quantized in these monolayers. Previous *ab initio* works [46,47] on germanene and stanene reported a quantized spin Hall conductivity. Our results show that it could be accidental that the spin Hall conductivity of germanene is close to the quantization value, i.e., 1.05 ($e/4\pi$). We do not observe the same quantization for stanene, silicene, and plumbene. We argued that the reason for this discrepancy is the coupling to the remote bands as well as contributions from other points of the Brillouin zone such as the gamma point. Another reason could be the use of a different method by Ref. [47] for the calculation of the spin Hall conductivity. The results also suggest that silicene, germanene, and stanene are suitable for applications involving the topological phase transition, whereas plumbene, due to the absence of a critical electric field, is more suitable for applications requiring a spin Hall effect that is robust to external fields. It should be noted that there are inherent limitations to the density functional theory such as the underestimation of the band gap which could, in principle, affect our numerical results. This limitation can be alleviated to an extent by including the self-energy using the GW method in the *ab initio* framework. However, the qualitative conclusions of this work are expected to remain the same. Moreover, verifying numerical results, such as the

value of the spin Hall conductivity, requires comparing theory with experimental data. However, since the spin Hall effect is difficult to observe directly, experiments involving indirect methods of measuring spin currents, such as the spin-torque ferromagnetic resonance method [66], will prove to be valuable in this regard.

[1] C. L. Kane and E. J. Mele, Phys. Rev. Lett. **95**, 226801 (2005).

[2] W.-F. Tsai, C.-Y. Huang, T.-R. Chang, H. Lin, H.-T. Jeng, and A. Bansil, Nat. Commun. **4**, 1500 (2013).

[3] M. Ezawa, J. Phys. Soc. Jpn. **84**, 121003 (2015).

[4] F. Geissler, J. C. Budich, and B. Trauzettel, New J. Phys. **15**, 085030 (2013).

[5] F.-F. Zhu, W.-J. Chen, Y. Xu, C.-L. Gao, D.-D. Guan, C.-H. Liu, D. Qian, S.-C. Zhang, and J.-F. Jia, Nat. Mater. **14**, 1020 (2015).

[6] J. Yuhara, B. He, N. Matsunami, M. Nakatake, and G. Le Lay, Adv. Mater. **31**, 1901017 (2019).

[7] A. Molle, J. Goldberger, M. Houssa, Y. Xu, S.-C. Zhang, and D. Akinwande, Nat. Mater. **16**, 163 (2017).

[8] K. S. Novoselov, A. K. Geim, S. V. Morozov, D. Jiang, M. I. Katsnelson, I. V. Grigorieva, S. V. Dubonos, and A. A. Firsov, Nature (London) **438**, 197 (2005).

[9] B. Lalmi, H. Oughaddou, H. Enriquez, A. Kara, S. Vizzini, B. Ealet, and B. Aufray, Appl. Phys. Lett. **97**, 223109 (2010).

[10] P. Vogt, P. De Padova, C. Quaresima, J. Avila, E. Frantzeskakis, M. C. Asensio, A. Resta, B. Ealet, and G. Le Lay, Phys. Rev. Lett. **108**, 155501 (2012).

[11] A. Fleurence, R. Friedlein, T. Ozaki, H. Kawai, Y. Wang, and Y. Yamada-Takamura, Phys. Rev. Lett. **108**, 245501 (2012).

[12] C.-L. Lin, R. Arafune, K. Kawahara, N. Tsukahara, E. Minamitani, Y. Kim, N. Takagi, and M. Kawai, Appl. Phys. Express **5**, 045802 (2012).

[13] M. E. Dávila, L. Xian, S. Cahangirov, A. Rubio, and G. Le Lay, New J. Phys. **16**, 095002 (2014).

[14] C.-H. Lin, A. Huang, W. W. Pai, W.-C. Chen, T.-Y. Chen, T.-R. Chang, R. Yukawa, C.-M. Cheng, C.-Y. Mou, I. Matsuda, T.-C. Chiang, H.-T. Jeng, and S.-J. Tang, Phys. Rev. Mater. **2**, 024003 (2018).

[15] J. Deng, B. Xia, X. Ma, H. Chen, H. Shan, X. Zhai, B. Li, A. Zhao, Y. Xu, W. Duan, S.-C. Zhang, B. Wang, and J. G. Hou, Nat. Mater. **17**, 1081 (2018).

[16] J. Yuhara, Y. Fujii, K. Nishino, N. Isobe, M. Nakatake, L. Xian, A. Rubio, and G. Le Lay, 2D Mater. **5**, 025002 (2018).

[17] S.-C. Wu, G. Shan, and B. Yan, Phys. Rev. Lett. **113**, 256401 (2014).

[18] Z. Yu, H. Pan, and Y. Yao, Phys. Rev. B **92**, 155419 (2015).

[19] Y. Xu, B. Yan, H.-J. Zhang, J. Wang, G. Xu, P. Tang, W. Duan, and S.-C. Zhang, Phys. Rev. Lett. **111**, 136804 (2013).

[20] N. Pournaghavi, M. Esmaeilzadeh, A. Abrishamifar, and S. Ahmadi, J. Phys.: Condens. Matter **29**, 145501 (2017).

[21] M. Ezawa, Phys. Rev. B **87**, 155415 (2013).

[22] L. L. Tao and E. Y. Tsymbal, Phys. Rev. B **100**, 161110(R) (2019).

[23] L. L. Tao, A. Naeemi, and E. Y. Tsymbal, Phys. Rev. Appl. **13**, 054043 (2020).

[24] S. Rachel and M. Ezawa, Phys. Rev. B **89**, 195303 (2014).

[25] M. Ezawa, Phys. Rev. Lett. **109**, 055502 (2012).

[26] H. Li, X. Wang, and A. Manchon, Phys. Rev. B **93**, 035417 (2016).

[27] A. V. Gert, M. O. Nestoklon, and I. N. Yassievich, J. Exp. Theor. Phys. **123**, 851 (2016).

[28] D. Kochan, S. Irmer, and J. Fabian, Phys. Rev. B **95**, 165415 (2017).

[29] C.-C. Liu, H. Jiang, and Y. Yao, Phys. Rev. B **84**, 195430 (2011).

[30] C.-C. Liu, W. Feng, and Y. Yao, Phys. Rev. Lett. **107**, 076802 (2011).

[31] L. C. Lew Yan Voon, A. Lopez-Bezanilla, J. Wang, Y. Zhang, and M. Willatzen, New J. Phys. **17**, 025004 (2015).

[32] S. Li and L. Zhang, Mater. Res. Express **6**, 025031 (2018).

[33] K. Takeda and K. Shiraishi, Phys. Rev. B **50**, 14916 (1994).

[34] S. Cahangirov, M. Topsakal, E. Aktürk, H. Şahin, and S. Ciraci, Phys. Rev. Lett. **102**, 236804 (2009).

[35] H. Şahin, S. Cahangirov, M. Topsakal, E. Bekaroglu, E. Akturk, R. T. Senger, and S. Ciraci, Phys. Rev. B **80**, 155453 (2009).

[36] N. D. Drummond, V. Zólyomi, and V. I. Fal'ko, Phys. Rev. B **85**, 075423 (2012).

[37] Z. Ni, Q. Liu, K. Tang, J. Zheng, J. Zhou, R. Qin, Z. Gao, D. Yu, and J. Lu, Nano Lett. **12**, 113 (2012).

[38] L. Matthes, O. Pulci, and F. Bechstedt, J. Phys.: Condens. Matter **25**, 395305 (2013).

[39] P. Rivero, J.-A. Yan, V. M. García-Suárez, J. Ferrer, and S. Barraza-Lopez, Phys. Rev. B **90**, 241408(R) (2014).

[40] G. Rahman, Europhys. Lett. **105**, 37012 (2014).

[41] H. Zhao, W.-X. Ji, C.-W. Zhang, P. Li, F. Li, P.-J. Wang, and R.-W. Zhang, Phys. Chem. Chem. Phys. **18**, 31862 (2016).

[42] X.-L. Yu, L. Huang, and J. Wu, Phys. Rev. B **95**, 125113 (2017).

[43] K. Yang, W.-Q. Huang, W. Hu, G.-F. Huang, and S. Wen, arXiv:1802.00591.

[44] M. Kurpas, P. E. Faria Junior, M. Gmitra, and J. Fabian, Phys. Rev. B **100**, 125422 (2019).

[45] A. Mahmood and G. Rahman, J. Phys.: Condens. Matter **32**, 205501 (2020).

[46] L. Matthes, S. Küfner, J. Furthmüller, and F. Bechstedt, Phys. Rev. B **94**, 085410 (2016).

[47] F. Matusalem, M. Marques, L. K. Teles, L. Matthes, J. Furthmüller, and F. Bechstedt, Phys. Rev. B **100**, 245430 (2019).

[48] L. Matthes and F. Bechstedt, Phys. Rev. B **90**, 165431 (2014).

[49] See Supplemental Material at http://link.aps.org/supplemental/10.1103/PhysRevB.104.115205 for the details of the symmetry analysis and the symmetry tables, which includes Ref. [67].

[50] E. Kogan, Graphene **2**, 74 (2013).

[51] P. Giannozzi *et al.*, J. Phys.: Condens. Matter **21**, 395502 (2009).

[52] P. Giannozzi *et al.*, J. Phys.: Condens. Matter **29**, 465901 (2017).

[53] P. E. Blöchl, Phys. Rev. B **50**, 17953 (1994).

[54] A. Dal Corso, Comput. Mater. Sci. **95**, 337 (2014).

[55] J. P. Perdew, K. Burke, and M. Ernzerhof, Phys. Rev. Lett. **77**, 3865 (1996).

[56] V. Sunko, H. Rosner, P. Kushwaha, S. Khim, F. Mazzola, L. Bawden, O. J. Clark, J. M. Riley, D. Kasinathan, M. W. Haverkort, T. K. Kim, M. Hoesch, J. Fujii, I. Vobornik, A. P. Mackenzie, and P. D. C. King, Nature (London) **549**, 492 (2017).

[57] R. Winkler and U. Zülicke, Phys. Rev. B **82**, 245313 (2010).

[58] M. Gradhand, D. V. Fedorov, F. Pientka, P. Zahn, I. Mertig, and B. L. Györffy, J. Phys.: Condens. Matter **24**, 213202 (2012).

[59] A. Dyrdał and J. Barnaś, Phys. Status Solidi RRL **6**, 340 (2012).

[60] M. Seemann, D. Ködderitzsch, S. Wimmer, and H. Ebert, Phys. Rev. B **92**, 155138 (2015).

[61] X. Wang, J. R. Yates, I. Souza, and D. Vanderbilt, Phys. Rev. B **74**, 195118 (2006).

[62] J. Qiao, J. Zhou, Z. Yuan, and W. Zhao, Phys. Rev. B **98**, 214402 (2018).

[63] J. H. Ryoo, C.-H. Park, and I. Souza, Phys. Rev. B **99**, 235113 (2019).

[64] G. Pizzi *et al.*, J. Phys.: Condens. Matter **32**, 165902 (2020).

[65] S. M. Farzaneh and S. Rakheja, Phys. Rev. Mater. **4**, 114202 (2020).

[66] L. Liu, T. Moriyama, D. C. Ralph, and R. A. Buhrman, Phys. Rev. Lett. **106**, 036601 (2011).

[67] M. S. Dresselhaus, G. Dresselhaus, and A. Jorio, *Group Theory: Application to the Physics of Condensed Matter* (Springer, Berlin, 2008).